Nakamura K, Moriyasu F, Tsuchida A, Kasuya K. Immunohistochemical analysis of p53 and MIB-1 in tissue specimens obtained from endoscopic ultrasonography-guided fine needle aspiration biopsy for the diagnosis of solid pancreatic masses. *Oncol Rep* 2005; **13**: 229-234 [PMID: 15643503]

19 **Kitoh H**, Ryozawa S, Harada T, Kondoh S, Furuya T, Kawauchi S, Oga A, Okita K, Sasaki K. Comparative genomic hybridization analysis for pancreatic cancer specimens obtained by endoscopic ultrasonography-guided fine-needle aspiration. *J Gastroenterol* 2005; **40**: 511-517 [PMID: 15942717 DOI: 10.1007/s00535-005-1577-0]

20 **Imaoka H**, Yamao K, Bhatia V, Shimizu Y, Yatabe Y, Koshikawa T, Kinoshita Y. Rare pancreatic neoplasms: the utility of endoscopic ultrasound-guided fine-needle aspiration-a large single center study. *J Gastroenterol* 2009; **44**: 146-153 [PMID: 19214677 DOI: 10.1007/s00535-008-2282-6]

21 **Sakamoto H**, Kitano M, Komaki T, Noda K, Chikugo T, Dote K, Takeyama Y, Das K, Yamao K, Kudo M. Prospective comparative study of the EUS guided 25-gauge FNA needle with the 19-gauge Trucut needle and 22-gauge FNA needle in patients with solid pancreatic masses. *J Gastroenterol Hepatol* 2009; **24**: 384-390 [PMID: 19032453 DOI: 10.1111/j.1440-1746.2008.05636.x]

22 **Yamao K**, Mizuno N, Takagi T, Hara K. How I do it and when I use (and do not use) EUS-FNA. *Gastrointest Endosc* 2009; **69**: S134-S137 [PMID: 19179139 DOI: 10.1016/j.gie.2008.12.020]

23 **Sugiyama M**, Hagi H, Atomi Y, Saito M. Diagnosis of portal venous invasion by pancreatobiliary carcinoma: value of endoscopic ultrasonography. *Abdom Imaging* 1997; **22**: 434-438 [PMID: 9157867 DOI: 10.1007/s002619900227]

24 **Gress FG**, Hawes RH, Savides TJ, Ikenberry SO, Cummings O, Kopecky K, Sherman S, Wiersema M, Lehman GA. Role of EUS in the preoperative staging of pancreatic cancer: a large single-center experience. *Gastrointest Endosc* 1999; **50**: 786-791 [PMID: 10570337 DOI: 10.1016/S0016-5107(99)70159-8]

25 **Ainsworth AP**, Rafaelsen SR, Wamberg PA, Durup J, Pless TK, Mortensen MB. Is there a difference in diagnostic accuracy and clinical impact between endoscopic ultrasonography and magnetic resonance cholangiopancreatography? *Endoscopy* 2003; **35**: 1029-1032 [PMID: 14648416 DOI: 10.1055/s-2003-44603]

26 **DeWitt J**, Devereaux B, Chriswell M, McGreevy K, Howard T, Imperiale TF, Ciaccia D, Lane KA, Maglinte D, Kopecky K, LeBlanc J, McHenry L, Madura J, Aisen A, Cramer H, Cummings O, Sherman S. Comparison of endoscopic ultrasonography and multidetector computed tomography for detecting and staging pancreatic cancer. *Ann Intern Med* 2004; **141**: 753-763 [PMID: 15545675]

27 **Ardengh JC**, Rosenbaum P, Ganc AJ, Goldenberg A, Lobo EJ, Malheiros CA, Rahal F, Ferrari AP. Role of EUS in the preoperative localization of insulinomas compared with spiral CT. *Gastrointest Endosc* 2000; **51**: 552-555 [PMID: 10805840 DOI: 10.1016/S0016-5107(00)70288-4]

28 **Iglesias-Garcia J**, Dominguez-Munoz JE, Abdulkader I, Larino-Noia J, Eugenyeva E, Lozano-Leon A, Forteza-Vila J. Influence of on-site cytopathology evaluation on the diagnostic accuracy of endoscopic ultrasound-guided fine needle aspiration (EUS-FNA) of solid pancreatic masses. *Am J Gastroenterol* 2011; **106**: 1705-1710 [PMID: 21483464 DOI: 10.1038/ajg.2011.119]

29 **Savoy AD**, Raimondo M, Woodward TA, Noh K, Pungpapong S, Jones AD, Crook J, Wallace MB. Can endosonographers evaluate on-site cytologic adequacy? A comparison with cytotechnologists. *Gastrointest Endosc* 2007; **65**: 953-957 [PMID: 17531627 DOI: 10.1016/j.gie.2006.11.014]

30 **Binmoeller KF**, Thul R, Rathod V, Henke P, Brand B, Jabusch HC, Soehendra N. Endoscopic ultrasound-guided, 18-gauge, fine needle aspiration biopsy of the pancreas using a 2.8 mm channel convex array echoendoscope. *Gastrointest Endosc* 1998; **47**: 121-127 [PMID: 9512275 DOI: 10.1016/S0016-5107(98)70343-8]

31 **Săftoiu A**, Vilmann P, Guldhammer Skov B, Georgescu CV. Endoscopic ultrasound (EUS)-guided Trucut biopsy adds significant information to EUS-guided fine-needle aspiration in selected patients: a prospective study. *Scand J Gastroenterol* 2007; **42**: 117-125 [PMID: 17190771 DOI: 10.1080/00365520600789800]

32 **Storch I**, Jorda M, Thurer R, Raez L, Rocha-Lima C, Vernon S, Ribeiro A. Advantage of EUS Trucut biopsy combined with fine-needle aspiration without immediate on-site cytopathologic examination. *Gastrointest Endosc* 2006; **64**: 505-511 [PMID: 16996340 DOI: 10.1016/j.gie.2006.02.056]

33 **Itoi T**, Itokawa F, Sofuni A, Nakamura K, Tsuchida A, Yamao K, Kawai T, Moriyasu F. Puncture of solid pancreatic tumors guided by endoscopic ultrasonography: a pilot study series comparing Trucut and 19-gauge and 22-gauge aspiration needles. *Endoscopy* 2005; **37**: 362-366 [PMID: 15824948 DOI: 10.1055/s-2004-826156]

34 **Varadarajulu S**, Fraig M, Schmulewitz N, Roberts S, Wildi S, Hawes RH, Hoffman BJ, Wallace MB. Comparison of EUS-guided 19-gauge Trucut needle biopsy with EUS-guided fine-needle aspiration. *Endoscopy* 2004; **36**: 397-401 [PMID: 15100946 DOI: 10.1055/s-2004-814316]

35 **Stewart CJ**, Coldewey J, Stewart IS. Comparison of fine needle aspiration cytology and needle core biopsy in the diagnosis of radiologically detected abdominal lesions. *J Clin Pathol* 2002; **55**: 93-97 [PMID: 11865001 DOI: 10.1136/jcp.55.2.93]

36 **Fornari F**, Civardi G, Cavanna L, Di Stasi M, Rossi S, Sbolli G, Buscarini L. Complications of ultrasonically guided fine-needle abdominal biopsy. Results of a multicenter Italian study and review of the literature. The Cooperative Italian Study Group. *Scand J Gastroenterol* 1989; **24**: 949-955 [PMID: 2688068]

37 **Paquin SC**, Gariépy G, Lepanto L, Bourdages R, Raymond G, Sahai AV. A first report of tumor seeding because of EUS-guided FNA of a pancreatic adenocarcinoma. *Gastrointest Endosc* 2005; **61**: 610-611 [PMID: 15812422]

38 **Chong A**, Venugopal K, Segarajasingam D, Lisewski D. Tumor seeding after EUS-guided FNA of pancreatic tail neoplasia. *Gastrointest Endosc* 2011; **74**: 933-935 [PMID: 21951481 DOI: 10.1016/j.gie.2010.10.020]

39 **Katanuma A**, Maguchi H, Hashigo S, Kaneko M, Kin T, Yane K, Kato R, Kato S, Harada R, Osanai M, Takahashi K, Shinohara T, Itoi T. Tumor seeding after endoscopic ultrasound-guided fine-needle aspiration of cancer in the body of the pancreas. *Endoscopy* 2012; **44** Suppl 2 UCTN: E160-E161 [PMID: 22622721 DOI: 10.1055/s-0031-1291716]

P- Reviewer Michalski C **S- Editor** Gou SX **L- Editor** Kerr C **E- Editor** Li JY

Maximum Standardized Uptake Value on FDG-PET Is a Strong Predictor of Overall and Disease-Free Survival for Non–Small-Cell Lung Cancer Patients after Stereotactic Body Radiotherapy

Atsuya Takeda, MD, PhD, Naoko Sanuki, MD,* Hirofumi Fujii, MD, PhD,† Noriko Yokosuka, MD,‡ Shuichi Nishimura, MD,* Yousuke Aoki, RTT,* Yohei Oku, PhD,* Yukihiko Ozawa, MD, PhD,‡ and Etsuo Kunieda, MD, PhD§*

Introduction: The maximum standardized uptake value (SUVmax) on ^{18}F-fluorodeoxyglucose positron emission tomography is a predictor for overall survival (OS) in non–small-cell lung cancer (NSCLC) after resection. We investigated the association between SUVmax and outcomes in NSCLC after stereotactic body radiotherapy.

Methods: Between 2005 and 2012, 283 patients with early NSCLC (T1a-2N0M0) were treated with stereotactic body radiotherapy; the total doses were 40 to 60 Gy in five fractions. Patients who underwent staging ^{18}F-fluorodeoxyglucose positron emission tomography scans by a single scanner and were followed up for more than or who died within 6 months were eligible. The optimal threshold SUVmax was calculated for each outcome. Outcomes were analyzed using the Kaplan–Meier method and log-rank test. Prognostic significance was assessed by univariate and multivariate analyses.

Results: One hundred fifty-two patients were eligible. Median follow-up was 25.3 (range, 1.3–77.4) months. Local, regional, and distant recurrences, cancer-specific deaths, and deaths from other reasons occurred in 14, 11, 27, 21, and 31 patients, respectively. The optimal threshold SUVmax for local, regional, and distant recurrences, and disease-free survival (DFS), cancer-specific survival, and OS were 2.47 to 3.64. Outcomes of patients with SUVmax lower than each threshold were significantly better than those with higher SUVmax (all $p<0.005$): 3-year DFS rates were 93.0% versus 58.3% ($p<0.001$) and 3-year OS rates were 86.5% versus 42.2% ($p<0.001$), respectively. By multivariate analysis, higher SUVmax was a significantly worse predictor for DFS ($p<0.01$) and OS ($p=0.04$).

Conclusions: SUVmax was a predictor for DFS and OS. A high SUVmax may be considered for intensive treatment to improve outcomes.

Key Words: ^{18}F-fluorodeoxyglucose positron emission tomography, Stage I non–small-cell lung cancer, Stereotactic body radiotherapy.

(*J Thorac Oncol.* 2014;9: 65–73)

For non–small-cell lung cancer (NSCLC), prognosis and therapy have been guided chiefly by the Tumor Node Metastasis staging system. Although stage I NSCLC patients have the best prognosis, their 5-year survival rate is approximately 60%.[1] Recently, ^{18}F-fluorodeoxyglucose (FDG) positron emission tomography (PET) imaging is widely used to determine Tumor Node Metastasis stage in NSCLC patients and is altering the stage designation and management in as many as 20% to 40% of patients.[2] A systematic review of resection in stage I NSCLC patients revealed that increased tumor FDG uptake is associated with worse survival.[3] These results suggest that FDG uptake can provide additional information about the biological characteristics of tumors that cannot be obtained by morphological imaging tests such as computed tomography (CT), and that it may be a potential biomarker for identifying stage I NSCLC patients with a high risk of recurrence or death.

Currently, stereotactic body radiation therapy (SBRT) is considered as a treatment option for patients with medically inoperable early-stage NSCLC.[4] We previously reported that maximum standardized uptake value (SUVmax) of primary tumors was a predictor for local control in NSCLC after SBRT.[5] In this study, herein we retrospectively investigated whether the SUVmax was a predictor for outcomes including disease-free survival (DFS) and overall survival (OS) after SBRT.

*Department of Radiology, Ofuna Chuo Hospital, Kamakura, Kanagawa, Japan; †Division of Functional Imaging, Research Center for Innovative Oncology, National Cancer Center Hospital East, Kashiwa, Japan; ‡Department of Radiology, Yuai Clinic, Yokohama, Japan; and §Department of Radiation Oncology, Tokai University School of Medicine, Isehara, Kanagawa, Japan.

Disclosure: Dr. Takeda is funded by Grant-in-Aid for Scientific Research (C) from the Japan Society for the Promotion of Science. Dr. Fujii is funded by Grants-in-Aid for Scientific Research (C) from the Japan Society for the Promotion of Science, Health and Labor Sciences Research Grants for Third Term Comprehensive 10-year Strategy for Cancer Control from the Ministry of Health, Labor and Welfare. The other authors declare no conflict of interest.

Address for correspondence: Hirofumi Fujii, MD, PhD, Division of Functional Imaging, Research Center for Innovative Oncology, National Cancer Center, 6-5-1 Kashiwanoha, Kashiwa 277–8577 Japan. E-mail: fujii-rad@umin.org

ISSN: 1556-0864/14/0901-0065

PATIENTS AND METHODS

Patients

From November 2005 through July 2012, 283 patients with early NSCLCs (T1a-2N0M0) and Eastern Cooperative Oncology Group performance status 0 to 2 were treated with SBRT: the total doses of 40 to 60 Gy in five fractions with radical intent. These patients had been diagnosed with NSCLC based on the following clinical findings: high SUVmax on FDG-PET scan, continuous tumor growth and characteristic findings on CT images and/or increases in tumor markers such as carcinoembryonic antigen, carbohydrate antigen 19-9, sialyl Lewis X-i antigen, squamous cell carcinoma antigen and cytokeratin 19 fragment. These diagnoses were completed after reaching a consensus among radiation oncologists, diagnostic radiologists, thoracic surgeons, and pulmonologists. Reasons for unproven histology included failed pathological studies, increased risk of hemorrhage during biopsy, patients' refusals, or technical difficulties during biopsy attempt. Among all 283 patients, 235 (83.0%) underwent ^{18}F-FDG-PET scans for staging before treatment. For this study, eligible patients underwent ^{18}F-FDG-PET scans before treatment by a single scanner at Yuai Clinic. Those who were lost to follow-up during the 6 months after treatment were excluded from the present analysis, except for patients who died.

This retrospective study was approved by the ethics committee at our institution (No. 2010-005). Written informed consent was obtained from patients for the staging tests, treatment, and follow-up studies.

FDG-PET and Data Analysis

Each patient underwent FDG-PET before SBRT. After fasting for 6 hours, FDG 3.5 MBq/kg body weight was intravenously injected if the patient's blood sugar level was lower than 200 mg/dl. Image acquisition was started 60 minutes after the injection by using a single PET/CT combined scanner (Eminence-SOPHIA, Shimadzu, Kyoto, Japan).[6] Image emission data from the eyes to the mid-thigh area were continuously acquired over a period of approximately 20 minutes. After attenuation corrections were made for the obtained image data, they were reconstructed using a dynamic row-action expectation maximization algorithm.[7] Then, the reconstructed sectional images were evaluated visually and quantitatively by using the SUVmax inside a volume of interest (VOI) placed on the lesions. SUVmax was calculated by: [(maximum activity in VOI)/(volume of VOI)]/[(injected FDG dose)/(patient weight)]. The quality of radiation measurements of the PET/CT scanner was assured by the calibration in accordance with an National Electrical Manufacturers Association (NEMA) NU-2 2001 standard.[8]

Treatment

We have previously reported the details about our SBRT technique.[9,10] Before 2011, treatment for central and peripheral NSCLC was planned to enclose the planning target volume (PTV) by the 80% isodose-line of the maximum dose with a total dose of 40 Gy and 50 Gy in five fractions, which was equivalent to the prescribed dose. From 2011, it was by the 60% isodose-line with 60 Gy and 50 Gy in five fractions[10] and, for cases where the target lesions were located adjacent to a critical organ, such as a main bronchus, pulmonary artery, esophagus, or heart, or extensively adhered to chest wall, the total dose was reduced by 10 Gy. The dose covering 95% of the PTV (D95) was more than or equal to the prescribed dose.[9] In our definition of treatment dose, the biologically effective doses assuming α/β ratios of 10 Gy (BED10) for the prescribed doses of 40 Gy, 50 Gy, and 60 Gy in five fractions at the PTV surface were 72 Gy_10, 100 Gy_10, and 132 Gy_10, respectively, and those at the maximum dose points were 100 Gy_10, 141 Gy_10, and 300 Gy_10, respectively.

No adjuvant chemotherapy was performed in any patient.

Follow-Up

Our follow-up procedures were previously described in detail.[11] In brief, all patients were followed up monthly during the first 6 months. CT scans were performed at 1 and 3 months after SBRT and at 3-month intervals during the first 2 years thereafter. Subsequently, follow-up interviews and CT scans were obtained at 4- to 6-month intervals. In addition, FDG-PET and brain magnetic resonance imaging were performed 1 year after SBRT.

Local recurrence was diagnosed by pathological confirmation or an increase of more than 25% in the cross-sectional tumor size on successive CT scans at least three times over a 6-month period. Regional and distant recurrence was defined as new appearance of mediastinal or hilar lymph node and distant metastasis, respectively. For DFS, only recurrence was counted as an event and death from other reasons was censored.

Statistical Analysis

The distributions of SUVmax in patients with pathologically and clinically diagnosed NSCLC were compared using the Student's t test. Differences in control and survival rates were compared by using Kaplan–Meier curves and log-rank tests. The predictive performance of SUVmax was assessed by receiver-operating characteristic curves and total area under the curve (AUC). Optimal thresholds were determined by calculating minimum balanced error rates. The 95% confidence interval for sensitivity, specificity, and AUC were calculated. Univariate and multivariate Cox regression analyses were used to determine whether any of the clinical or treatment-related variables were predictors of local control. Univariate factors with p value less than 0.20 were included in the multivariate analysis. For all tests, a p value less than 0.05 was considered statistically significant. Analyses were performed using IBM SPSS Statistics 20.0 (IBM, Inc., Armonk, NY).

RESULTS

Eligible Patients and Those Outcomes

From a total of 283 NSCLC patients treated with SBRT, 152 patients were eligible for this study (Fig. 1), including 90 patients with pathologically proven NSCLC and 62 patients with clinically diagnosed NSCLC. Among patients

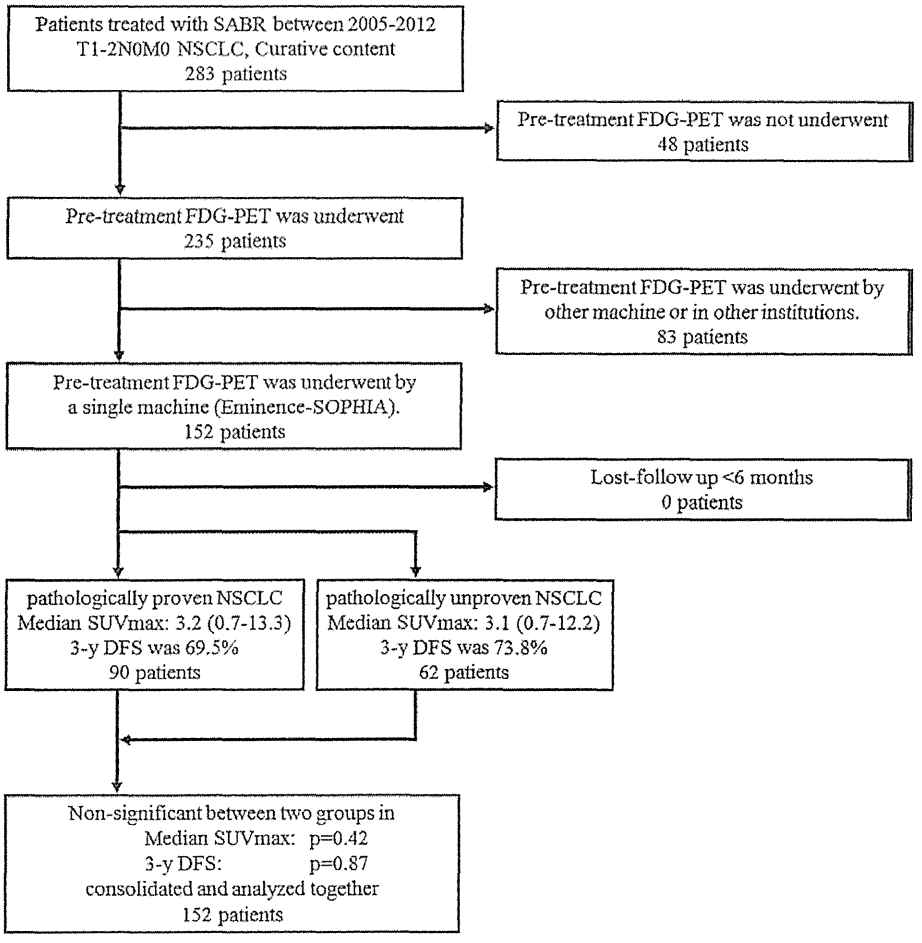

FIGURE 1. Study flow chart.

with clinically diagnosed NSCLC, SUVmaxs were more than 2.5 in 42 patients (68%) and tumor marker levels were elevated in 34 patients (55%). Patient characteristics are shown in Table 1. Median patient age was 79 years (range, 53–90 years). The median follow-up period was 25.3 months (range, 1.3–77.4 months). Three patients died because of causes other than NSCLC within 6 months.

On FDG-PET studies, the median SUVmaxs in primary tumors of pathologically and clinically diagnosed NSCLC were 3.2 (range, 0.7–13.3) and 3.1 (range, 0.7–12.2), respectively; these values were not significantly different (p=0.42). Three-year DFS rates for patients with pathologically and clinically diagnosed NSCLC were 69.5% and 73.8%, respectively; these rates were also not significantly different (p=0.87; Fig. 2). Therefore, we consolidated the data for these patients and analyzed them together.

Local, regional nodal, and distant recurrences occurred in 14, 11, and 27 patients, respectively. There were 21 cause-specific deaths and 31 deaths from other reasons.

^{18}F-FDG-PET/CT SUVmax as Predictors of Outcome

The median SUVmax of the primary lesion in patients with recurrence/death and nonrecurrence/alive, AUC on receiver-operating characteristic curves, the optimal threshold SUVmax, and its sensitivity and specificity for outcomes are shown in Table 2. Patients with SUVmax less than threshold for local, regional nodal, and distant metastasis controls, and for DFS, cancer-specific survival, and OS were significantly better than those with SUVmax more than threshold (p<0.005). The median blood glucose level (mg/dl) was 97 (range, 77–192). Only four patients, including three who remain alive with no recurrence and one who died from distant metastasis, had blood sugar levels exceeding 150 mg/dl. The patient who died was correctly classified under the poor prognosis group.

Figure 3 shows Kaplan–Meier curves for DFS, cancer-specific survival, and OS divided by the most optimal threshold SUVmax, which were 2.47, 2.55, and 2.55, respectively.

Univariate and Multivariate Analysis for Predictors of DFS and OS

The results of univariate and multivariate analyses for DFS and OS are shown in Table 3. The univariate analyses showed that tumor diameter, T stage, and SUVmax were significantly related to DFS, and that body mass index (BMI), tumor diameter, T stage, and SUVmax were significantly related to OS. Body mass index (BMI), tumor diameter,

TABLE 1. Patient and Tumor Characteristics

Characteristic	*n*
Median age (range), yrs	79 (53–90)
Sex: male/female	109/43
Median SUVmax (range)	3.2 (0.7–13.3)
Median follow-up duration (range), months	25.3 (1.3–77.4)
BMI (range)	21.1 (12.7–37.6)
Operability: yes/no	39/113
Median maximum tumor diameter (range), cm	2.5 (1.0–6.2)
T stage:[a] T1a/ T1b / T2	56/53/43
Pathology	
Pathology-proven NSCLC	
Adenocarcinoma	52
Squamous cell carcinoma	28
Unclassified NSCLC	10
Pathologically unproven	62
Tumor opacity	
Solid	130
GGO	6
GGO with solid	16
Location: central/peripheral	41/111
Total dose: 40 Gy/50 Gy/60 Gy	26/106/20

SUVmax, the maximum standardized uptake value; BMI, body mass index; NSCLC, non–small-cell lung cancer; GGO, ground-glass opacity.
[a]All patients were stage N0,M0.

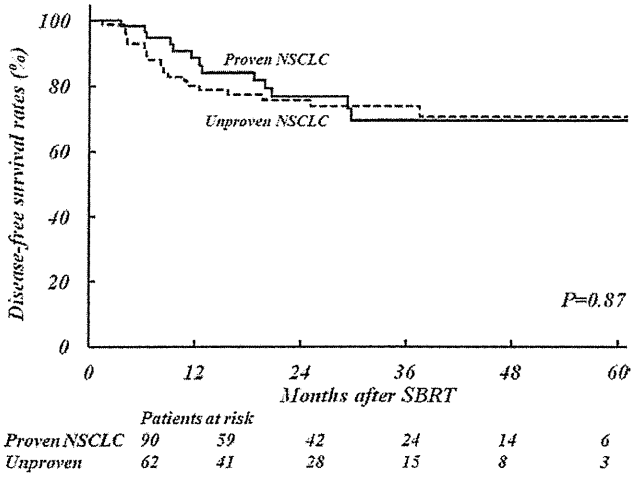

FIGURE 2. Disease-free survival rates of candidate patients with and without pathological confirmation. There is no difference in disease-free survival rates between patients with and without pathological confirmation of non–small-cell lung cancer (p=0.87).

T stage, and SUVmax were significantly related to OS. In multivariate analysis, we excluded tumor diameter because the correlation coefficient (r) between tumor diameter and T stage exceeded 0.9. Multivariate analysis indicated that only SUVmax was significantly associated with DFS. BMI, T stage, pathological confirmation, and SUVmax were significantly related to OS.

DISCUSSION

A meta-analysis conducted by the European Lung Cancer Working Party identified 13 studies examining FDG uptake and prognosis for patients with stage I–III NSCLC who underwent resection. They found that the hazard of death was twice as great in patients with high FDG uptake compared with those with low FDG uptake (hazard ratio 2.09).[12] In addition, another systematic review of patients with stage I NSCLC also suggested that higher FDG uptake was associated with worse DFS and OS.[3] Across studies, the median DFS or OS was 70% for patients with higher FDG uptake compared with 88% for patients with lower FDG uptake.[3] FDG uptake has the potential to be used as a biomarker for identifying stage I patients who are at increased risk of death or recurrence and therefore could identify candidates for participation in future trials of adjuvant therapy.

For SBRT, only a few reports with relatively small numbers of patients have evaluated FDG uptake as a potential biomarker. The utility of FDG uptake as a biomarker remains controversial. However, two studies positively associated FDG uptake with survival by multivariate analysis: Chang et al.[13] reported that SUVmax was the only predictor for OS, with a hazard ratio of 2.15 divided at the median SUVmax, and Clarke et al.[14] also reported SUVmax as the only predictor for DFS. Meanwhile, two univariate analysis studies failed to establish a significant association between FDG uptake and survival.[15,16]

In the present study, we clearly demonstrated that SUVmax was a strong predictor for all outcomes, including control of local, regional nodal, and distant metastasis, DFS, and OS. By multivariate analysis, SUVmax as well as T stage were independent predictors for OS. The two factors seemed to influence cancer-specific survival. Other factors associated with OS included BMI and pathological confirmation. They also seemed to influence death from other causes, because both factors were not predictors of DFS, even by univariate analysis. NSCLC patients often have emphysema as a comorbidity, and low BMI was correlated with short OS in patients with emphysema.[17] Patients with clinically diagnosed NSCLC might include benign other disease than NSCLC and have better outcomes. In addition, the pathological diagnosis of ground-glass opacities was not often established although most of the cases were likely to be bronchoalveolar carcinoma. It was reported that their SUVmaxs were as low as a median value of 0.6 and they showed better outcomes.[18] and have better outcomes. Therefore, we at first demonstrated that there was no significant difference in distribution of SUVmax (p=0.42) and DFS (p=0.87; Fig. 2) between patients with pathologically and clinically diagnosed NSCLC. However, lack of pathological confirmation was a worse predictor of OS, as was shown in a German multicenter analysis.[19] It might indicate patients' inactive performance status or comorbid disease, because physicians might hesitate to perform an invasive biopsy in such patients.

On the basis of these results, we suggest the use of more intensive treatment for medically inoperable stage I NSCLC.

TABLE 2. Relationships between the Maximum Standardized Uptake Value and Clinical Outcomes

	SUVmax < Threshold	SUVmax > Threshold	*p* Value
Local control, *n*	78	74	
AUC (95% CI)	0.78 (0.66–0.91)		<0.001
Threshold SUVmax	3.35		
Sensitivity/specificity	0.93/0.56		
3-yr local control rate	97.7%	71.5%	<0.001
Regional control, *n*	90	62	
AUC (95% CI)	0.78 (0.67–0.89)		0.002
Threshold SUVmax	3.64		
Sensitivity/specificity	0.91	0.63	
3-yr regional control rate	98.6%	78.6%	<0.001
Distant metastasis control, *n*	59	93	
AUC (95% CI)	0.58 (0.48–0.69)		0.18
Threshold SUVmax	2.47		
Sensitivity/specificity	0.85/0.44		
3-yr distant metastasis– free rate	96.0%	66.7%	0.002
Disease-free survival, *n*	59	93	
AUC (95% CI)	0.68 (0.58–0.77)		0.001
Threshold SUVmax	2.47		
Sensitivity/specificity	0.89/0.47		
3-yr disease-free survival rate	93.0%	58.3%	<0.001
Cancer-specific survival, *n*	60	92	
AUC (95% CI)	0.68 (0.58–0.79)		0.01
Threshold SUVmax	2.55		
Sensitivity/specificity	0.95/0.45		
3-yr cancer-specific survival rate	100%	61.5%	<0.001
Overall survival, *n*	60	92	
AUC (95% CI)	0.71 (0.62–0.79)		<0.001
Threshold SUVmax	2.55		
Sensitivity/specificity	0.85/0.52		
3-yr overall survival rate	86.5%	42.2%	<0.001

SUVmax, maximum standardized uptake value; AUC, area under the curve on receiver-operating characteristic curves; CI, confidence interval.

First, to improve local control, dose escalation might be required. A large single-institution series suggested a positive dose-control relationship for SBRT.[20] Another single-institution series suggested that the local control rate could be improved by securing the minimum dose for PTV.[21] In the German multicenter analysis, multivariate analysis revealed that PTV-encompassing dose was a significant factor for local control and OS. This result indicated that intensified SBRT with the consequence of improved local tumor control transfers into improved OS.[19] Second, we should seek optimal treatment to decrease regional node and distant metastasis, which are the main causes of cancer death after SBRT.[22] SBRT candidates are medically inoperable, elderly and/or with comorbidities. For such patients, it is doubtful whether systemic chemotherapy would prolong OS. However, for completely resected stage IB NSCLC patients, systemic chemotherapy with uracil-tegafur significantly increased OS rate.[23] Although the role of platinum-based adjuvant chemotherapy in patients with stage IB has not been established, further randomized trials for select patients are required using biological markers.[24] Recently, combination chemo-radiotherapy was reported to provide a clinically significant benefit over radiotherapy alone in a select group of elderly patients with locally advanced NSCLC.[25] Therefore, mild systemic chemotherapy might have a potential role in patients with a high SUVmax and relatively good performance status.

SUVmax is an index that can be obtained by rather simple calculations. Therefore, based on the results of the present study, we can insist that oncologists should more actively use ^{18}F-FDG-PET/CT testing and calculate the SUVmax of lesions in clinical practice of SBRT for early-stage NSCLC. As a result, SUVmax would be a popular imaging biomarker for patients with this disease. However, SUV is not an absolutely reliable quantitative index. For example, it is reported that obtained SUVmaxs depend on the imaging protocols and scanners used,[26] uptake time[27] and respiratory motion especially in studies about lung cancer.[28] Therefore, it is not suitable to directly apply our results to other institutes. To use

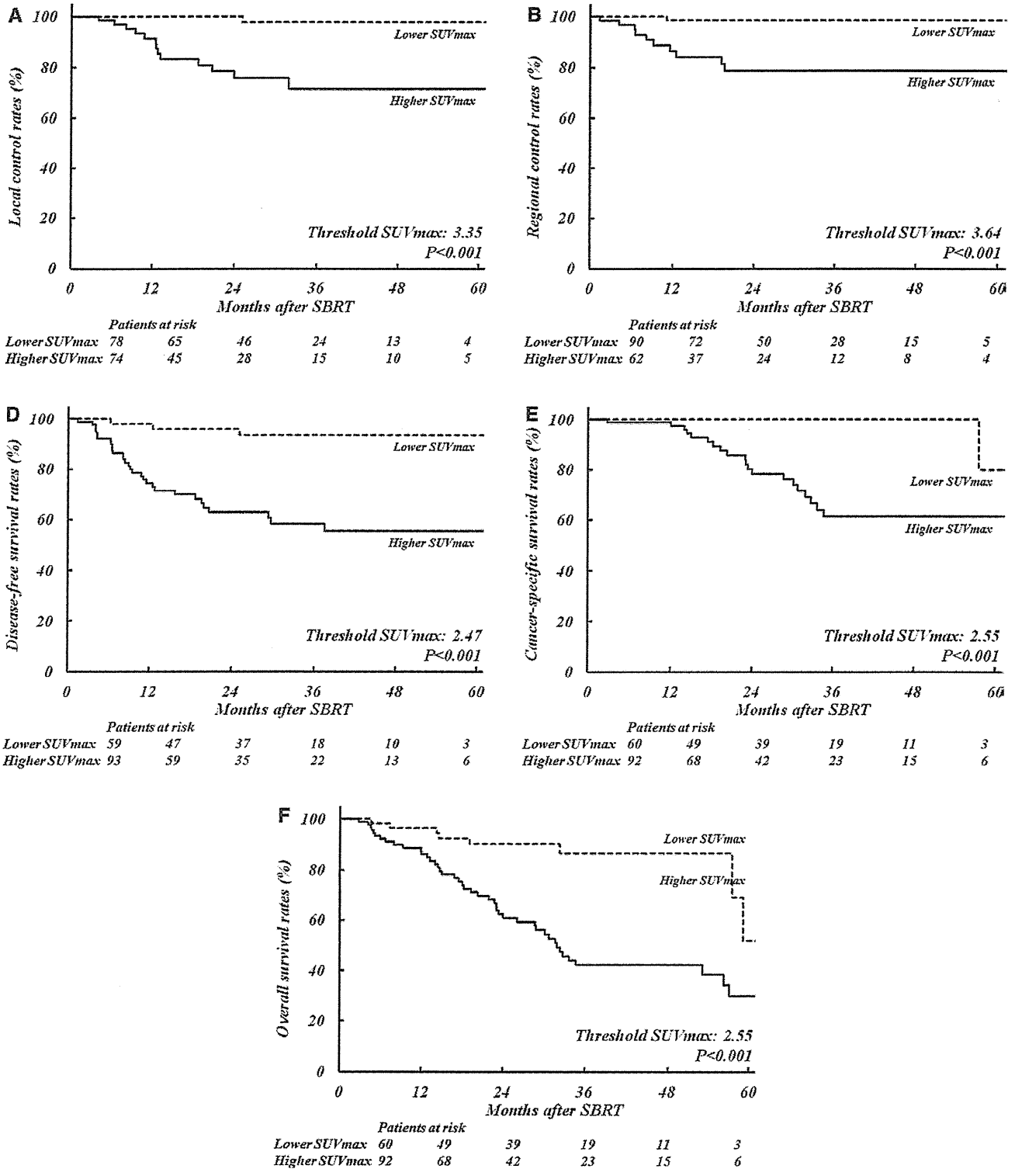

FIGURE 3. Clinical outcomes of patients divided by each threshold maximum standardized uptake value. Kaplan–Meier curves show that all the outcomes of patients with an SUVmax lower than the threshold value are significantly better than those with higher SUVmax. *A*, Local control rate, (*B*) regional node control rate, (C), distant metastasis–free rate, (*D*) disease-free survival rate, (*E*) cancer-specific survival rate, and (*F*) overall survival rate.

TABLE 3. Univariate and Multivariate Analysis for Disease-Free and Overall Survival

	Disease-Free Survival			Overall Survival		
Characteristic	**HR**	**95% CI**	***p* Value**	**HR**	**95% CI**	***p* Value**
Univariate analysis						
Age	1.04	0.99–1.10	0.16	1.04	1.00–1.09	0.08
Sex			0.41			0.24
Male (*n*=109)	1.00			1.00		
Female (*n*=43)	0.74	0.37–1.50		0.67	0.34–1.31	
BMI	0.99	0.89–1.09	0.75	0.90	0.8–0.99	0.02*
Operability			0.27			0.19
Yes (*n*=37)	1.00			1.00		
No (*n*=105)	0.65	0.68–3.97		1.58	0.79–3.16	
Maximum diameter	1.98	1.45–2.69	<0.01*	1.45	1.11–1.90	<0.01*
T stage			0.01*			0.01*
T1a (*n*=56)	1.00			1.00		
T1b (*n*=53)	3.90	1.52–10.0	<0.01*	2.78	1.40–5.52	<0.01*
T2 (*n*=43)	3.70	1.40–9.75	<0.01*	2.10	1.01–4.40	0.05
Location			0.28			0.71
Peripheral (*n*=104)	1.00			1.00		
Central (*n*=38)	1.47	0.73–2.97		1.13	0.61–2.09	
Total dose			0.21			0.58
40 Gy (*n*=23)	1.00			1.00		
50 Gy (*n*=119)	0.50	0.23–1.08	0.08	0.70	0.35–1.41	0.32
60 Gy (*n*=23)	0.68	0.18–2.54		0.62	0.13–2.88	0.54
Pathologically proven			0.87			0.08
Yes (*n*=90)	1.00			1.00		
No (*n*=62)	0.95	0.48–1.86		1.64	0.95–2.83	
Pathology			0.42			0.23
Adenocarcinoma (*n*=52)	1.00			1.00		
SCC (*n*=28)	1.92	0.74–4.97	0.18	1.67	0.70–3.98	0.25
NOS (*n*=10)	2.32	0.71–7.53	0.16	1.58	0.51–4.91	0.43
Unproven (*n*=62)	1.33	0.58–3.08	0.50	2.06	1.04–4.08	0.04*
Tumor opacity			0.08			0.02*
Solid (*n*=130)	1.00			1.00		
GGO (with solid) (*n*=22)	0.28	0.07–1.16		0.19	0.05–0.78	
SUVmax			<0.01*			<0.01*
<Threshold[a] (*n*=59, 60)	1.00			1.00		
>Threshold[a] (*n*=93, 92)	6.25	2.20–17.732		4.18	1.97–8.87	<0.01*
Multivariate analysis						
Age	1.02	0.96–1.08	0.57	1.03	0.98–1.08	0.26
BMI				0.92	0.85–0.99	0.04*
Operability						0.34
Yes (*n*=37)				1.00		
No (*n*=105)				1.26	0.61–2.63	
T stage			0.06			0.04*
(*n*=56)	1.00			1.00		
T1b (*n*=53)	2.80	1.07–7.28	0.04*	2.54	1.24-5.22	0.01*
T2 (*n*=43)	3.16	1.17–8.54	0.02*	2.01	0.93-4.33	0.08
Pathological confirmation						0.04*
Yes (*n*=90)				1.00		
No (*n*=62)				1.83	1.03–3.26	
Tumor opacity			0.74			0.36
Solid (*n*=130)	1.00			1.00		

(Continued)

TABLE 3. *(Continued)*

	Disease-Free Survival			Overall Survival		
GGO (with solid; n=22)	0.73	0.12–4.50		0.48	0.10–2.36	
SUVmax			<0.01*			0.04*
<Threshold[a] (n=59, 60)	1.00			1.00		
>Threshold[a] (n=93, 92)	5.94	1.58–22.35		2.46	1.03–5.91	

[a] For disease-free survival, the SUVmax threshold, the number of patients with the SUVmax <threshold and >threshold were 2.47, 59, and 93, respectively. For overall survival, these were 2.55, 60, and 92, respectively.

HR, hazard ratio; CI, confidence interval; BMI, body mass index; SCC, squamous cell carcinoma; NOS, not otherwise specified; GGO, ground-glass opacity; SUVmax, maximum standardized uptake value.

* p<0.05.

SUVmax as a reliable biomarker in clinical practice in many institutions, researchers in the field of nuclear medicine are making efforts for the standardization procedures.[29] For example, European Association of Nuclear Medicine published a guideline to facilitate the standardization of tumor PET imaging[30] and European Association of Nuclear Medicine Research Ltd. started a program to accredit imaging sites that meet these standard requirements. Similar projects are also planned in other areas.[31] In the future, the issue of interinstitutional differences would be improved.

Limitations

This study had several limitations, including a short follow-up period, limited sample size, and its retrospective nature. In this study, 39.5% of tumors were not pathologically confirmed. Reasons for the lack of pathology data included negative biopsy studies and the inability to perform biopsies because of medical comorbidities or patient refusal. Accordingly, pathological nonconfirmation was one of the worse predictors for OS. However, other studies have also reported the results of SBRT after obtaining 31% to 51% pathologic confirmation of malignancy.[32,33] In addition, the treatment outcomes of patients diagnosed with NSCLC with no pathological confirmation were almost identical to those of patients with pathological confirmation.[34,35]

CONCLUSIONS

In conclusion, multivariate analysis revealed that the SUVmax of a primary tumor was the only prognostic factor for DFS, and that it was the strongest prognostic factor for OS in addition to BMI, T stage, and pathological confirmation. Further studies are required to ascertain whether SUVmax might have an impact on changing treatment strategies, including dose escalation and adjuvant therapies, and, accordingly, on improving patient outcomes.

REFERENCES

1. Rami-Porta R, Ball D, Crowley J, et al.; International Staging Committee; Cancer Research and Biostatistics; Observers to the Committee; Participating Institutions. The IASLC Lung Cancer Staging Project: proposals for the revision of the T descriptors in the forthcoming (seventh) edition of the TNM classification for lung cancer. *J Thorac Oncol* 2007;2:593–602.
2. van Tinteren H, Hoekstra OS, Smit EF, et al. Effectiveness of positron emission tomography in the preoperative assessment of patients with suspected non-small-cell lung cancer: the PLUS multicentre randomised trial. *Lancet* 2002;359:1388–1393.
3. Nair VS, Krupitskaya Y, Gould MK. Positron emission tomography 18F-fluorodeoxyglucose uptake and prognosis in patients with surgically treated, stage I non-small cell lung cancer: a systematic review. *J Thorac Oncol* 2009;4:1473–1479.
4. Chi A, Liao Z, Nguyen NP, Xu J, Stea B, Komaki R. Systemic review of the patterns of failure following stereotactic body radiation therapy in early-stage non-small-cell lung cancer: clinical implications. *Radiother Oncol* 2010;94:1–11.
5. Takeda A, Yokosuka N, Ohashi T, et al. The maximum standardized uptake value (SUVmax) on FDG-PET is a strong predictor of local recurrence for localized non-small-cell lung cancer after stereotactic body radiotherapy (SBRT). *Radiother Oncol* 2011;101:291–297.
6. Matsumoto K, Kitamura K, Mizuta T, et al. Performance characteristics of a new 3-dimensional continuous-emission and spiral-transmission high-sensitivity and high-resolution PET camera evaluated with the NEMA NU 2-2001 standard. *J Nucl Med* 2006;47:83–90.
7. Kitamura K, Ishikawa A, Mizuta T, et al. 3D continuous emission and spiral transmission scanning for high-throughput whole-body PET. *Nuclear Science Symposium Conference Record, 2004 IEEE*. 2004;5:2801–2805.
8. Association NEM. *Performance Measurements of Positron Emission Tomographs. NEMA Standards Publication NU 2-2001*. Rosslyn, VA: NEMA; 2001.
9. Takeda A, Kunieda E, Sanuki N, et al. Dose distribution analysis in stereotactic body radiotherapy using dynamic conformal multiple arc therapy. *Int J Radiat Oncol Biol Phys* 2009;74:363–369.
10. Oku Y, Takeda A, Kunieda E, et al. Analysis of suitable prescribed isodose line fitting to planning target volume in stereotactic body radiotherapy using dynamic conformal multiple arc therapy. *Practical Radiation Oncology* 2011;2:46–53.
11. Takeda A, Kunieda E, Takeda T, et al. Possible misinterpretation of demarcated solid patterns of radiation fibrosis on CT scans as tumor recurrence in patients receiving hypofractionated stereotactic radiotherapy for lung cancer. *Int J Radiat Oncol Biol Phys* 2008;70:1057–1065.
12. Berghmans T, Dusart M, Paesmans M, et al.; European Lung Cancer Working Party for the IASLC Lung Cancer Staging Project. Primary tumor standardized uptake value (SUVmax) measured on fluorodeoxyglucose positron emission tomography (FDG-PET) is of prognostic value for survival in non-small cell lung cancer (NSCLC): a systematic review and meta-analysis (MA) by the European Lung Cancer Working Party for the IASLC Lung Cancer Staging Project. *J Thorac Oncol* 2008;3:6–12.
13. Chang JY, Liu H, Balter P, et al. Clinical outcome and predictors of survival and pneumonitis after stereotactic ablative radiotherapy for stage I non-small cell lung cancer. *Radiat Oncol* 2012;7:152.
14. Clarke K, Taremi M, Dahele M, et al. Stereotactic body radiotherapy (SBRT) for non-small cell lung cancer (NSCLC): is FDG-PET a predictor of outcome? *Radiother Oncol* 2012;104:62–66.
15. Burdick MJ, Stephans KL, Reddy CA, Djemil T, Srinivas SM, Videtic GM. Maximum standardized uptake value from staging FDG-PET/CT does not predict treatment outcome for early-stage non-small-cell lung cancer treated with stereotactic body radiotherapy. *Int J Radiat Oncol Biol Phys* 2010;78:1033–1039.
16. Satoh Y, Nambu A, Onishi H, et al. Value of dual time point F-18 FDG-PET/CT imaging for the evaluation of prognosis and risk factors for

recurrence in patients with stage I non-small cell lung cancer treated with stereotactic body radiation therapy. *Eur J Radiol* 2012;81:3530–3534.
17. Landbo C, Prescott E, Lange P, Vestbo J, Almdal TP. Prognostic value of nutritional status in chronic obstructive pulmonary disease. *Am J Respir Crit Care Med* 1999;160:1856–1861.
18. Chun EJ, Lee HJ, Kang WJ, et al. Differentiation between malignancy and inflammation in pulmonary ground-glass nodules: The feasibility of integrated (18)F-FDG PET/CT. *Lung Cancer* 2009;65:180–186.
19. Guckenberger M, Allgäuer M, Appold S, et al. Safety and efficacy of stereotactic body radiotherapy for stage i non-small-cell lung cancer in routine clinical practice: a patterns-of-care and outcome analysis. *J Thorac Oncol* 2013;8:1050–1058.
20. McCammon R, Schefter TE, Gaspar LE, Zaemisch R, Gravdahl D, Kavanagh B. Observation of a dose-control relationship for lung and liver tumors after stereotactic body radiation therapy. *Int J Radiat Oncol Biol Phys* 2009;73:112–118.
21. Shirata Y, Jingu K, Koto M, et al. Prognostic factors for local control of stage I non-small cell lung cancer in stereotactic radiotherapy: a retrospective analysis. *Radiat Oncol* 2012;7:182.
22. Nath SK, Sandhu AP, Kim D, et al. Locoregional and distant failure following image-guided stereotactic body radiation for early-stage primary lung cancer. *Radiother Oncol* 2011;99:12–17.
23. Kato H, Ichinose Y, Ohta M, et al.; Japan Lung Cancer Research Group on Postsurgical Adjuvant Chemotherapy. A randomized trial of adjuvant chemotherapy with uracil-tegafur for adenocarcinoma of the lung. *N Engl J Med* 2004;350:1713–1721.
24. Borghaei H, Mehra R, Simon G. Current issues in adjuvant chemotherapy for resected, stage IB non-small-cell lung cancer. *Future Oncol* 2009;5:19–22.
25. Atagi S, Kawahara M, Yokoyama A, et al.; Japan Clinical Oncology Group Lung Cancer Study Group. Thoracic radiotherapy with or without daily low-dose carboplatin in elderly patients with non-small-cell lung cancer: a randomised, controlled, phase 3 trial by the Japan Clinical Oncology Group (JCOG0301). *Lancet Oncol* 2012;13:671–678.
26. Thie JA. Understanding the standardized uptake value, its methods, and implications for usage. *J Nucl Med* 2004;45:1431–1434.
27. Schillaci O. Use of dual-point fluorodeoxyglucose imaging to enhance sensitivity and specificity. *Semin Nucl Med* 2012;42:267–280.
28. Kawano T, Ohtake E, Inoue T. Deep-inspiration breath-hold PET/CT of lung cancer: maximum standardized uptake value analysis of 108 patients. *J Nucl Med* 2008;49:1223–1231.
29. Scheuermann JS, Saffer JR, Karp JS, Levering AM, Siegel BA. Qualification of PET scanners for use in multicenter cancer clinical trials: the American College of Radiology Imaging Network experience. *J Nucl Med* 2009;50:1187–1193.
30. Boellaard R, O'Doherty MJ, Weber WA, et al. FDG PET and PET/CT: EANM procedure guidelines for tumour PET imaging: version 1.0. *Eur J Nucl Med Mol Imaging* 2010;37:181–200.
31. Daisaki H, Tateishi U, Terauchi T, et al. Standardization of image quality across multiple centers by optimization of acquisition and reconstruction parameters with interim FDG-PET/CT for evaluating diffuse large B cell lymphoma. *Ann Nucl Med* 2013;27:225–232.
32. Lagerwaard FJ, Haasbeek CJ, Smit EF, Slotman BJ, Senan S. Outcomes of risk-adapted fractionated stereotactic radiotherapy for stage I non-small-cell lung cancer. *Int J Radiat Oncol Biol Phys* 2008;70:685–692.
33. van der Voort van Zyp NC, Prévost JB, Hoogeman MS, et al. Stereotactic radiotherapy with real-time tumor tracking for non-small cell lung cancer: clinical outcome. *Radiother Oncol* 2009;91:296–300.
34. Verstegen NE, Lagerwaard FJ, Haasbeek CJ, Slotman BJ, Senan S. Outcomes of stereotactic ablative radiotherapy following a clinical diagnosis of stage I NSCLC: comparison with a contemporaneous cohort with pathologically proven disease. *Radiother Oncol* 2011;101:250–254.
35. Takeda A, Kunieda E, Sanuki N, Aoki Y, Oku Y, Handa H. Stereotactic body radiotherapy (SBRT) for solitary pulmonary nodules clinically diagnosed as lung cancer with no pathological confirmation: comparison with non-small-cell lung cancer. *Lung Cancer* 2012;77:77–82.

Medical Physics
The International Journal of Medical Physics Research and Practice

Blood vessel-based liver segmentation using the portal phase of an abdominal CT dataset

Ahmed S. Maklad, Mikio Matsuhiro, Hidenobu Suzuki, Yoshiki Kawata, Noboru Niki, Mitsuo Satake, Noriyuki Moriyama, Toru Utsunomiya, and Mitsuo Shimada

Citation: Medical Physics **40**, 113501 (2013); doi: 10.1118/1.4823765
View online: http://dx.doi.org/10.1118/1.4823765
View Table of Contents: http://scitation.aip.org/content/aapm/journal/medphys/40/11?ver=pdfcov
Published by the American Association of Physicists in Medicine

Blood vessel-based liver segmentation using the portal phase of an abdominal CT dataset

Ahmed S. Maklad
Systems Innovation Engineering, Graduate School of Advanced Technology and Science, The University of Tokushima, Tokushima 770-8506, Japan

Mikio Matsuhiro, Hidenobu Suzuki, Yoshiki Kawata, and Noboru Niki[a)]
Institute of Technology and Science, the University of Tokushima, Tokushima 770-8506, Japan

Mitsuo Satake
National Cancer Center Hospital East, Kashiwa, Chiba 277-8577, Japan

Noriyuki Moriyama
Tokyo Midtown Clinic, Minato-ku, Tokyo 107-6206, Japan

Toru Utsunomiya and Mitsuo Shimada
Institute of Health Biosciences, the University of Tokushima, Tokushima 770-8503, Japan

(Received 7 March 2013; revised 12 September 2013; accepted for publication 12 September 2013; published 11 October 2013)

Purpose: Blood vessel (BV) information can be used to guide body organ segmentation on computed tomography (CT) imaging. The proposed method uses abdominal BVs (ABVs) to segment the liver through the portal phase of an abdominal CT dataset. This method aims to address the wide variability in liver shape and size, separate liver from other organs of similar intensity, and segment hepatic low-intensity tumors (LITs).

Methods: Thin ABVs are enhanced using three-dimensional (3D) opening. ABVs are extracted and classified into hepatic BVs (HBVs) and nonhepatic BVs (non-HBVs) with a small number of interactions, and HBVs and non-HBVs are used for constraining automatic liver segmentation. HBVs are used to individually segment the core region of the liver. To separate the liver from other organs, this core region and non-HBVs are used to construct an initial 3D boundary surface. To segment LITs, the core region is classified into non-LIT- and LIT-parts by fitting the histogram of the core region using a variational Bayesian Gaussian mixture model. Each part of the core region is extended based on its corresponding component of the mixture, and extension is completed when it reaches a variation in intensity or the constructed boundary surface, which is reconfirmed to fit robustly between the liver and neighboring organs of similar intensity. A solid-angle technique is used to refine main BVs at the entrances to the inferior vena cava and the portal vein.

Results: The proposed method was applied to 80 datasets: 30 Medical Image Computing and Computer Assisted Intervention (MICCAI) and 50 non-MICCAI; 30 datasets of non-MICCAI data include tumors. Our results for MICCAI-test data were evaluated by sliver07 (http://www.sliver07.org/) organizers with an overall score of 85.7, which ranks best on the site as of July 2013. These results (average $\pm$ standard deviation) include the five error measures of the 2007 MICCAI workshop for liver segmentation as follows. Results for volume overlap error, relative volume difference, average symmetric surface distance, root mean square symmetric surface distance, and maximum symmetric surface distance were 4.33 $\pm$ 0.73, 0.28 $\pm$ 0.87, 0.63 $\pm$ 0.16, 1.19 $\pm$ 0.28, and 14.01 $\pm$ 2.88, respectively; and when applying our method to non-MICCAI data, results were 3.21 $\pm$ 0.75, 0.06 $\pm$ 1.29, 0.45 $\pm$ 0.17, 0.98 $\pm$ 0.26, and 12.69 $\pm$ 3.89, respectively. These results demonstrate high performance of the method when applied to different CT datasets.

Conclusions: BVs can be used to address the wide variability in liver shape and size, as BVs provide unique details for the structure of each studied liver. Constructing a boundary surface using HBVs and non-HBVs can separate liver from its neighboring organs of similar intensity. By fitting the histogram of the core region using a variational Bayesian Gaussian mixture model, LITs are segmented and measuring the volumetry of non-LIT- and LIT-parts becomes possible. Further examination of the proposed method on a large number of datasets is required for clinical applications, and development of the method for full automation may be possible and useful in the clinic. © *2013 American Association of Physicists in Medicine*. [http://dx.doi.org/10.1118/1.4823765]

Key words: liver segmentation, blood vessel (BV), boundary surface, computed tomography (CT) dataset, portal phase

1. INTRODUCTION

Liver segmentation is the basis for computer-based planning of surgical interventions.[1,2] Accurate preoperative estimates of graft weight are imperative to avoid small-for-size syndrome in the recipient and ensure donor safety after adult living donor liver transplantations.[1] Preoperative detailed topography as well as precise liver resection volume measurements should be obtained for curative hepatectomies.[2]

Manual segmentation is available clinically, but it is a tedious and time-consuming process that by its nature is not reproducible.[1] Nonmanual approaches for segmenting the liver are either automatic, semiautomatic, or interactive. Automatic approaches are desirable and have an additional advantage to semiautomatic and interactive methods in that automatic approaches have no user interactions; however, semiautomatic and interactive approaches remain essential for clinical settings especially with a very deformable organ like the liver.

For a comparison of different algorithms to segment the liver from clinical three-dimensional (3D) CT scans, Heimman *et al.*[3] started an investigation of 3D segmentation in the clinic: A grand challenge workshop in conjunction with Medical Image Computing and Computer Assisted Intervention (MICCAI) 2007. In this workshop, originally pathological CT scans from a variety of different CT scanners were acquired in the portal phase. Identical reference data and evaluation tools were applied for all algorithms.

Ten automatic and six interactive algorithms were evaluated, compared to each other and their results published.[3] The workshop is over, but the liver segmentation competition continues through the website (www.sliver07.org).

A comprehensive review of different techniques for liver segmentation based on CT images was done by Campadelli *et al.*,[5] describing different methods and techniques for liver segmentation along with their drawbacks.

Through MICCAI workshop comparisons and this comprehensive review, liver segmentation methods and techniques are based on live wire segmentation,[6,7] gray-level based methods,[3,8] neural networks,[9] model-fitting techniques,[4,10–18] probabilistic atlases,[14,19–22] level-set approaches,[23–25] two-dimensional region growing,[26] neighborhood-connected region-growing (NCRG),[27] and graph cut based approaches.[28–37] Some of the techniques are developed or integrated with others achieving better results when compared with their individual results.

Live-wire segmentation approaches divide the liver through a set of seed points chosen manually to determine the boundary of the liver.[6] This technique is combined with Radial bias functions and level sets to segment the liver semiautomatically,[7] achieving rank 2 (84.6) on sliver07 (April 2013). With the live-wire technique, the user has full control over the segmentation process. As a consequence, the resulting segmentation is heavily dependent on the operator's skill, potentially limiting accuracy because of possible individual errors and biases.[5]

With gray-level based methods, liver gray levels are estimated through statistical analysis of some slices segmented manually or by histogram analysis in a gray level range. An iterative threshold is applied to further create a binary volume in 2D or 3D. Morphological operations are applied to eliminate attached organs. These methods do not take into account the wide variability of CT volumes.[5]

Neural network-based methods use the gray level features corresponding to the liver for segmentation. The networks learn three patterns: liver, liver boundary, and nonliver patterns. Then, morphological operations, boundary detection by Laplacian filtering, and B-spline curves are used to refine boundaries. Those techniques are likely to fail when two neighboring organs have similar intensities.[5]

Statistical shape models (SSMs) are model-fitting techniques frequently used for segmenting the liver. In a comparative study,[3] shape-constrained segmentation methods were matched with SSMs, a technique that requires a large amount of training data to construct an SSM fitting with different liver shapes. However, SSMs are much harder to model when working with highly complex and variable shapes such as the liver.[4,5] Kainmuller *et al.*[11] automatically segmented the liver through a combination of a constrained free-form model with a statistical deformable model around the liver boundary, achieving the best score (77.3) for automatic segmentation on sliver07 website (April 2013). Wimmer *et al.*[12] proposed a probabilistic active shape model and applied it for liver segmentation achieving the second best score (76.8) for automatic segmentation on the site (April 2013).

Probabilistic atlases are constructed through the deposition of a large amount of training computed tomography (CT) data into a standard space defined by a small number of landmarks. The atlas is created by a spatial averaging of the registered organs.[5] Compared with shape models, atlas-based methods appear to have more problems in adapting to the wide variability in shape and size of livers.[3]

Level set approaches segment the liver based on a novel speed function.[5] The user has to draw rough contours inside the liver in a number of transverse slices to initialize level set evolution. This initialization employs a novel definition of the speed function. However, stopping the level set evolution based on standard terms is not reliable due to the low contrast between tissue types.[3]

Neighborhood connected region growing is used for segmenting the liver from the portal phase of a CT dataset. A liver region is initialized to be used as a seed region. From this region, the liver is segmented using NCRG. Dilation is then used to overcome undersegmentation. However, other organs of intensity similar to the liver could not be separated and low intensity tumors were undersegmented.[27]

Graph-cut approaches for liver segmentation are extensions of Boykov graph cuts.[20,21] Beichel *et al.*[22] uses the graph-cut approach as an initial segmentation of the liver followed by an interactive refinement step to overcome merged organs with liver and undersegmentation of tumors with different gray values, achieving the fourth best score (82.1) for semiautomatic segmentation on the site (April 2013) with a running time of 36 min.[3,30] Afifi *et al.*[31] integrate shape and statistical information of the liver with a graph-cuts algorithm to segment the liver semiautomatically achieving the fifth best

score (81.8) on the site (April 2013). Linguraru *et al.*[35,37] combined different techniques to segment the liver automatically. Liver is initialized based on an atlas using adaptive enhancement estimations. A fast marching level set is applied to grow the segmentation. A geodesic contour is applied to refine the segmentation result. Graph cut is applied to segment hepatic tumors. This approach achieved the third best score (76.2) for automatic segmentation on the site (April 2013) with a running time 50–60 min.[37]

The literature yields numerous examples of the various drawbacks associated with liver segmentation from the portal phase of a CT dataset. These problems include: (1) wide variability of anatomic structures of the liver in shape and size;[3,21,27,38] (2) insufficient separation on CT images of other abdominal organs of similar intensity to the liver;[1,23,24,38,39] and (3) undersegmentation of low-intensity tumors (LITs).[27,38,40–42]

Blood vessels (BVs) provide unique details for each liver in terms of organ shape and size. Therefore, we propose a method that uses abdominal blood vessel (ABV), hepatic blood vessel (HBV), and non-HBV, information to constrain liver segmentation from the portal phase of a CT dataset aiming at addressing the aforementioned issues.[43,44] Saitoh *et al.* used HBVs to segment the liver.[45] Therefore, their method is expected to take into consideration the wide variability of liver shapes and sizes. However, these authors did not clarify the capability of their method at separating liver from other neighboring organs of similar intensity and segmenting LITs.

Our proposed method differs from this approach[45] at many points: (1) for segmenting the liver core region, the proposed method applied Delaunay triangulation using end points of HBVs and intensity of CT image, not HBVs itself as used in Saitoh *et al.*, (2) for separating the liver from other organs, the proposed method uses HBVs, non-HBVs, the heart, and bones information to construct a boundary surface fitting robustly between the liver and other organs of similar intensity, not by erosion and dilation as in Saitoh *et al.*, and (3) for segmenting LITs, the proposed method fits the histogram of the core region using a variational Bayesian Gaussian mixture model, whereas in Saitoh *et al.* segmenting LITs is not mentioned at all.

We trained our method using 20 MICCAI training datasets and present the results of testing this method using 10 MICCAI-test datasets for an adequate comparison with the literature, and 50 non-MICCAI datasets from Tokushima University Hospital. The proposed segmentation technique allows volumetric information about the liver and hepatic tumors as well as HBVs vascular tree in the liver and connections with main ABVs. This information may help surgeons at planning different hepatic surgeries.

2. MATERIALS AND METHODS

The idea proposed here is to segment the liver semiautomatically based on BV information taken from only the portal phase of an abdominal CT dataset. This segmentation is achieved in two stages. First, ABVs are extracted and classified into HBVs and non-HBVs with a small number of interactions (Sec. 2.B). This extraction of BVs is just an initialization step to find the core region of the liver and some external boundaries that will drive final liver segmentation. Second, HBVs and non-HBVs are used to constrain the automatic segmentation of the liver (Sec. 2.C).

2.A. Materials

A contrast-enhanced CT scan usually consists of triphasic evaluation, including an arterial phase, a portal venous phase, and an equilibrium phase. The portal venous phase of a CT scan is acquired 50–70 s after initiation of contrast media administration, and clearly shows hepatic portal branches.[46]

The method herein uses the portal phase. In this phase, the liver parenchyma is enhanced, portal and hepatic vein enhancement is higher than the liver parenchyma, common tumors are less enhanced than liver parenchyma, some tumors are more enhanced than the aorta,[47] kidneys, renal arteries, and veins are enhanced, the aorta is still enhanced, the inferior vena cava (IVC) is slightly enhanced, and the heart is enhanced. These characteristics of the portal phase may vary according to the time that the portal phase is achieved. In the late portal phase, the renal parenchyma has almost the same contrast as liver.

MICCAI training data (20 datasets) are used for training and setting different variables in the proposed method. Then, the performance of the method is tested using two databases: the MICCAI-test database (10 datasets) and the non-MICCAI database (50 datasets). MICCAI data (training and test) and reference labeling of training datasets were downloaded from the sliver07 website. All MICCAI datasets were enhanced with contrast agent and scanned in the central venous phase on a variety of scanners (different manufactures, 4, 16, and 64 detector rows). All datasets were acquired in the transversal direction. Pixel size spacing varied between 0.55 and 0.80 mm, the interslice distance varied from 1 to 3 mm. Most of these datasets were pathologic and included tumors, metastases and cysts of different sizes.[3,48] To generate reference segmentation for MICCAI data, radiological experts manually outlined liver contours for all datasets in the transverse plane in a slice-by-slice fashion.[3] Non-MICCAI data are 50 contrast-enhanced multislice abdominal CT datasets at the portal phase from Tokushima University Hospital, Tokushima, Japan. These data contain 20 normal and 30 abnormal datasets and collected following national privacy laws. Abnormal datasets contain 45 tumors of different sizes [average maximum length, 38.2 mm; standard deviation (SD), 21.1 mm], with 13 tumors adjoined to the liver boundary and 32 located inside the liver. These datasets were acquired using a Toshiba Aquilion scanner (Toshiba Medical Systems, Otawara-shi, Tochigi, Japan; tube current: 100–360 mA; tube voltage: 120 kV; reconstruction functions: FC01, FC13; one scan time: 0.5 s). Slice thickness was 1 mm. Each slice had a size of 512 × 512 pixels, and pixel size ranged from 0.546 to 0.683 mm. The 3D coordinate system had the Z-axis parallel to the body axis and oriented from the topmost to the bottommost slice. X- and Y-axes were oriented along the width from right to left and the height from bottom

to top of the axial slice, respectively. MICCAI training and test data have one reference for each dataset. We obtained one reference for each dataset of non-MICCAI data as well. For obtaining this reference, two experts with five years experience in CT image analysis segmented livers in these datasets. Each expert was assigned 25 datasets to segment the liver manually in the transverse plane in a slice-by-slice fashion. Segmentation results of each expert are checked by the other. When there was a disagreement about a liver contour at any region, the two experts discussed and corrected the liver contour at the variability region. The final results were one reference data for each dataset. This reference is used for evaluation of the non-MICCAI data.

2.B. Extraction of ABVs and subsequent classification into HBVs and non-HBVs

2.B.1. Extraction of ABVs

Extraction of ABVs from CT images is achieved in three steps: (1) removal of bone, accumulated calcium, and kidneys; (2) enhancement of peripheral BVs; and (3) extraction of ABVs.

2.B.1.a. Step 1: Removal of bone, accumulated calcium, and kidneys. Image noise is reduced using a median filter [Fig. 1(a)].[49] A review of the MICCAI training data revealed that ABVs and the liver (e.g., liver and tumor tissues) are in the range of 0–350 Hounsfield units (HU). Bone and accumulated calcium (if any) are extracted by applying a threshold technique with a value greater than 350 HU. Labels of volume < 1 mm^3 are deleted from the threshold result. Kidneys are extracted using seeded region-growing (SRG).[50] The user chooses manually a seed point at a high intensity region of the renal cortex of the right kidney. Automatically, this seed point is replaced by a 2D-region centered at the seed point with a radius of 2 mm. The mean intensity (HU) of points in this region is obtained. The region grows connecting points with intensity more than or equal to this mean. The volumetry of this region growing result (V_1) is measured. Next, region growing is repeated with intensity 3 HU lower than the first mean. This process is repeated iteratively, decreasing the mean each time by 3 HU. The volumetry of each region growing result (V_i) is measured. The difference in volume between two consecutive iterations is measured as well. The region growing stops when $(V_i - V_{i-1})/V_{i-1} \geq 0.2$, and $V_{i-1} > 0$ where $i = 2, 3, 4$, etc. The value 0.2 is chosen experimentally based on a review of MICCAI-training data to avoid region growing leakage into neighboring organs. The left kidney is extracted in the same method. In late portal phase case, the region growing for extracting kidneys may leak into the liver through the vena cava. The user corrects this leakage by first deleting manually the label of a slice of the vena cava between the right renal vein and the liver, and second applying an erosion operation of radius 1 mm to the result and selecting the region that is connected with the seed point of the right kidney. A dilation of 1 mm followed by a closing operation[51] of 2 mm is applied to the extracted regions to cover bone, accumulated calcium (if any), and kidneys [Fig. 1(b)]. Through changing the CT value at the closing result into a negative value, bone, accumulated calcium, and kidneys are removed [Fig. 1(c)]. Changing into a negative value results in a high level of variation in the intensity between the liver and these extracted regions. This variance in intensity prevents leaking of the liver into these regions during the liver-core-region extension process described in Sec. 2.C.

2.B.1.b. Step 2: Enhancement of peripheral BVs by two grayscale morphological operations. Anatomically, peripheral BVs and tissues have very small differences in intensity. To emphasize peripheral BVs, an opening in 3D is applied at regions > 0 HU. In this opening, two morphological operations (i.e., erosion and dilation) are applied consecutively with three radii with lengths of 1, 2, and 4 voxels. When the radius is equal to one voxel, the erosion operation requires that the central voxel takes the minimum value of its 3D surrounding voxels. At the dilation operation, the central voxel takes the maximum value among its own value and the values of its surrounding voxels. The result of this step is used as an input to the next. The operations diverge when the radius is less than or equal to two voxels: for erosion, all of the inside voxels take the minimum value of their outer boundary voxels, whereas for dilation, the inside voxels take the maximum value of their own values and the values of their surrounding voxels. The image that results from this corrective action can then be applied when the radius is ≤ 4 voxels (3 mm). This process obtains a blurred image (background) fitting adequately with tissues and BVs of radii > 3 mm.

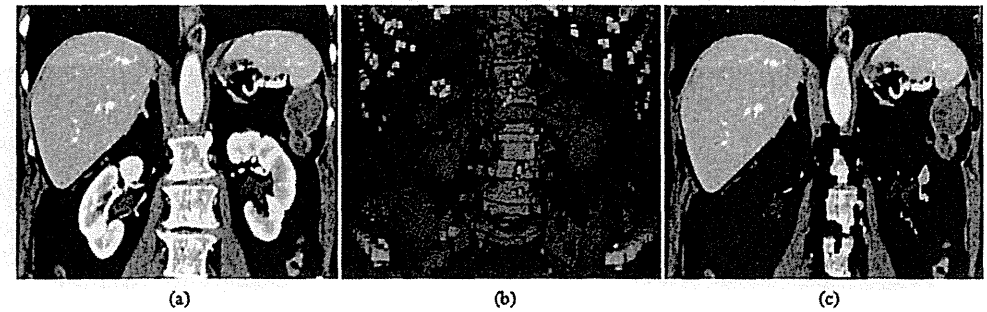

FIG. 1. Removal of bone, accumulated calcium, and kidneys. (a) Noise of original image is reduced using a median filter. (b) Bone and accumulated calcium are extracted through a threshold. Kidneys are extracted using a seeded region-growing. (c) Extracted regions are removed. Accumulated calcium is marked by an arrow.

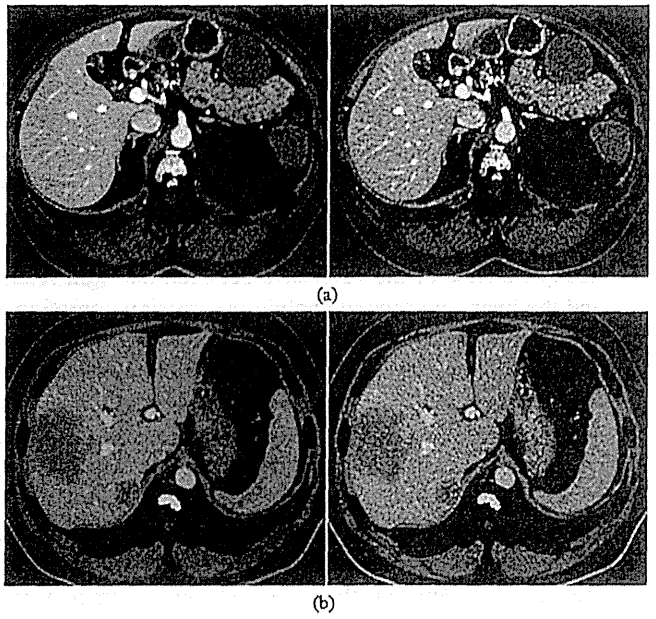

FIG. 2. Enhancement of peripheral blood vessels is achieved using 3D bias field correction. (Left) CT image before enhancement and (right) after enhancement. (a) A nonlow intensity tumor (NLIT) case (MICCAI-training-15) and (b) a LIT case (MICCAI-training-16).

By subtracting this background from the image that ensues from removal of bone, accumulated calcium, and the kidneys [Fig. 2(a, left)], peripheral BVs remain. These remaining peripheral BVs are added to the image in Fig. 2(a, left) enhancing peripheral BVs [Fig. 2(a, right)]. In LIT cases [Fig. 2(b)], this enhancement increases the extracted peripheral blood vessels that surrounds low intensity tumors in three dimensions.

2.B.1.c. Step 3: Extraction of ABVs. Using the enhanced BVs CT image (only at this step), a 3D seeded region growing technique is performed to extract ABVs. An axial section containing the entrance of the IVC is selected manually. The seed point is initialized manually at the entrance of the IVC [Fig. 3(a)]. To avoid any potential interuser variability in choosing the seed point, a 2D region centered at the chosen seed point with a radius of 6 mm is selected automatically. A histogram of this region is calculated. A threshold is set at the 75th percentile HU of the histogram [Fig. 3(b)]. Points in the selected region with intensity more than or equal to this threshold are the actual seed region for the region growing. This region grows in 3D to connect voxels having intensity more than or equal to the threshold. Volumetry of this region growing result (V_1) is measured. Next, the seed region grows connecting voxels with intensity 3 HU less than the threshold. This process is repeated iteratively, decreasing the intensity each time by 3 HU. The volumetry of each region growing result (V_i) is measured. The region growing stops when $((V_i - V_{i-1})/V_{i-1}) \geq 0.2$ and $V_{i-1} > 0$, where i = 2, 3, 4, etc.

ABVs of the majority of abdominal organs are extracted through this region growing [Fig. 3(c)]. A section of the heart is extracted with ABVs owing to its similarity in intensity with ABVs in the portal phase. In diseased cases, hepatic tumors with intensity close to ABVs (or high-intensity tumors) are also extracted. Extraction of a section of the heart and hepatic tumors with ABVs do not affect liver segmentation, as the hepatic tumors are reduced into points inside the liver when constructing the liver core region (Sec. 2.C), and as the extracted heart sections are classified as non-HBVs.

2.B.2. Classifying ABVs into HBVs and non-HBVs

Extracted BVs are classified into HBVs and non-HBVs in three steps: (1) removal of main BVs, proper hepatic artery, the heart, and high-intensity tumors; (2) clustering of medial and peripheral BVs; and (3) classification of HBVs and non-HBVs.

2.B.2.a. Step 1: Removal of main BVs, proper hepatic artery, the heart, and high-intensity tumors. ABVs and part of the heart are classified into different categories by assigning each voxel of the segmented vessel and heart a specific value. This value is decided according to the thickness of the vessel and heart component containing this voxel. This procedure was performed using a reverse-squared Euclidean distance transformation parallel type algorithm[52] [Fig. 4(a)]. These categories are assigned numbers in an ascending order from thinnest to thickest. For removing main connections between HBVs and non-HBVs, the user selects manually the number of the category associated with the thickest part of the main portal vein (the entrance of the portal vein to the liver). Deleting this category disconnects the entrance of the PV to the hepatic PV. However the proper hepatic artery will be still connecting the abdominal aorta and HBVs because it is thinner than the entrance of the PV. To disconnect the proper hepatic artery, main BVs that are assigned numbers greater than or equal to the selected number [Fig. 4(b)], are 3D-dilated by

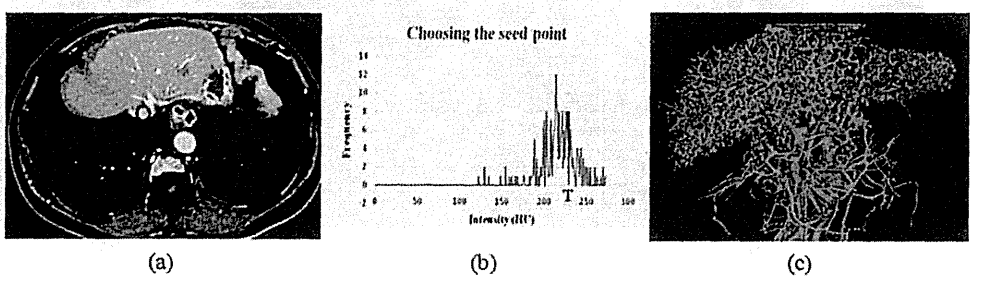

FIG. 3. Extraction of ABV: (a) an enhanced image (entrance of the inferior vena cava is marked with a circle), (b) 2D histogram of the region inside this circle (threshold value is marked with (T) which represents 75th percentile), and (c) extraction result.

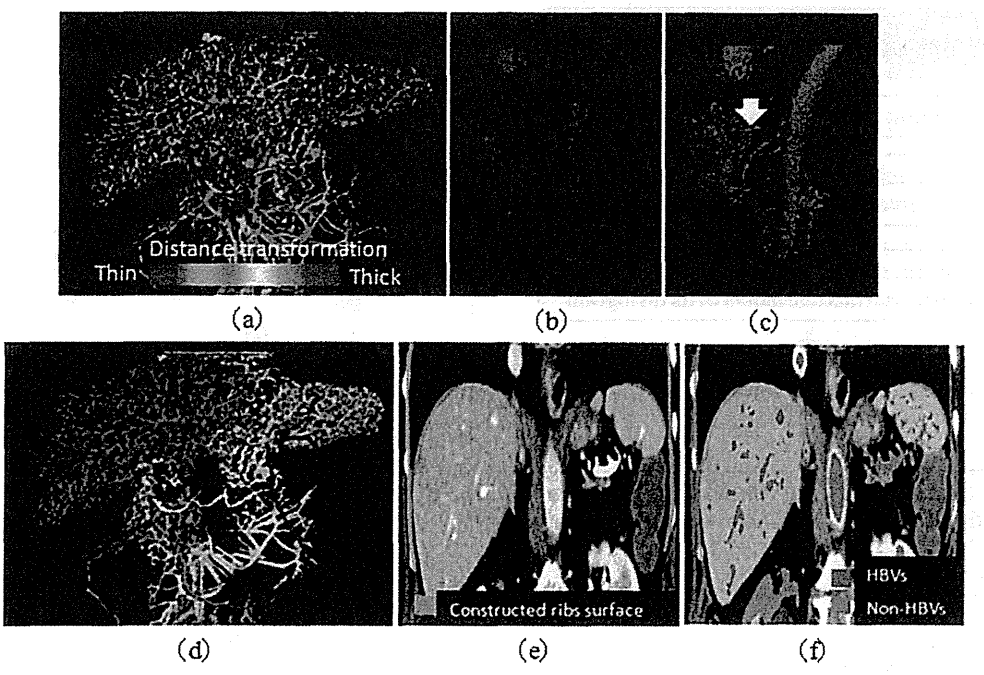

FIG. 4. Classification of HBVs and non-HBVs cluster: (a) extracted ABVs are classified into different labels by applying a distance transformation technique. (b) Main BV and parts of the heart are selected for dilation. (c) BVs of (a) that included at the region of dilating (b) are separated (proper hepatic artery is marked with an arrow). (d) Remaining BVs and parts of the heart are classified into different clusters. (e) Extracted ribs boundary surface and (f) HBVs and non-HBVs cluster are classified (ribs boundary surface, eroded main BV, the right kidney, the heart and accumulated calcium (if any) are added to the non-HBVs cluster).

10 mm. The result in Fig. 4(a) is overlapped with this dilation region. In the dilation region, main portal vein, proper hepatic artery, the entrance and exit of the IVC to the liver, the abdominal aorta, parts of the heart, and any extracted large high-intensity tumors (if any) are extracted [Fig. 4(c)]. The region in Fig. 4(c) is removed from the extracted BVs in Fig. 4(a), as shown in Fig. 4(d) resulting in removal of main connections of HBVs with non-HBV. In some cases, entrance or exit of the IVC to the liver is not separated from HBVs by this interaction. This is corrected through manually deleting the label of the IVC in two slices: one between HBVs and the heart and the other at the exit of the IVC from the liver.

2.B.2.b. Step 2: Clustering medial and peripheral BVs. By using the remaining vessels after separation of main BVs, medial and peripheral BVs are then classified into different categories in an ascending order from the thinnest to the thickest as we aforementioned. BVs with the first-order category are classified as peripheral BVs, where all other remaining BVs are classified as medial BVs. Peripheral BVs are separated from medial ones. Consequently, medial BVs of different organs become disconnected from each other. Through assigning a label to each connected group of BVs, medial BVs are obtained in different labels. Each label represents one cluster of medial BVs. Through checking connectivity of each peripheral BV with its neighboring clusters of medial BVs, peripheral BVs are classified into two clusters. The first cluster includes peripheral BVs that are connected to only one cluster of medial BVs. The second includes peripheral BVs that are connected into two or more of medial BVs clusters. The second cluster of peripheral BVs is deleted completely to avoid connections between medial BVs clusters. The first cluster of peripheral BVs is added back to medial BVs clusters. In this way, clusters of medial and peripheral BVs of different organs are obtained [Fig. 4(d)].

2.B.2.c. Step 3: Classification of HBVs and non-HBVs. The liver is the largest abdominal organ and is located at the upper-right quadrant of the abdomen.[27,32] Based on this observation, HBVs are identified and assigned to the first cluster. To determine the largest abdominal organ, volumetries of medial and peripheral BVs clusters are calculated and arranged in descending order. To determine the upper-right quadrant of the abdomen, the center of gravity of each cluster is calculated. The center of a cluster is the average a_x and a_y of X- and Y-components of all voxels included in this cluster, respectively. A cluster is classified as HBVs when it satisfies two conditions simultaneously: it has the greatest volume and its center exists at the region where $a_x - a_y \leq 0$. This cluster is assigned to the first label. All other clusters are assigned to the second label forming the non-HBV cluster. The region in Fig. 4(c) is eroded 2 mm in 3D and added to the non-HBV cluster as well. This erosion keeps main BVs disconnected from HBVs. Bones are used to construct the ribs surface. Using extracted bones, the ribs are extracted.[53] A closing operation of radius 2 mm is applied to the extracted ribs. A technique based on a two-pass thinning algorithm[49] is applied to extract the ribs center lines. The ribs boundary surface is constructed through applying Delaunay triangulation[54] to connect the thinning results with a maximum length 50 mm [Fig. 4(e)]. This length is chosen experimentally to connect different ribs and minimize connection between parts of the same rib. This surface is added to the non-HBV cluster. Right kidney and accumulated calcium (if any) are added to the non-HBV cluster as well [Fig. 4(f)].

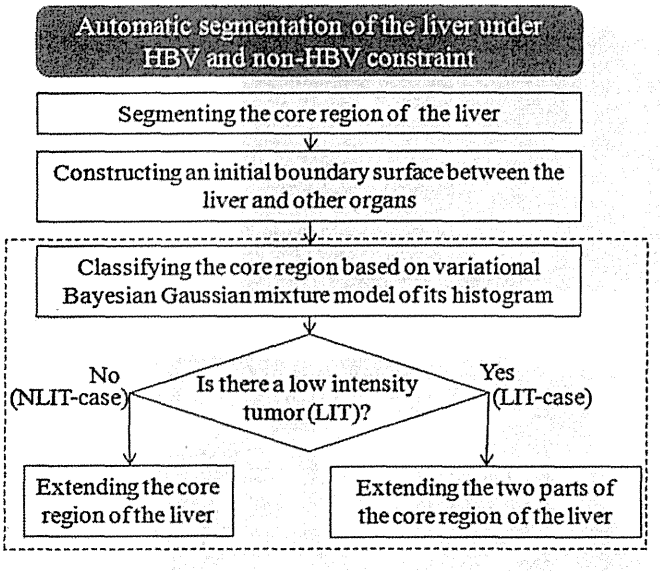

FIG. 5. Schematic diagram of the second stage of the proposed method.

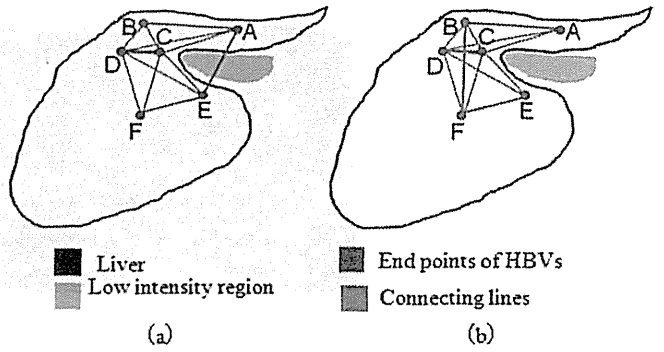

FIG. 6. Delaunay triangulation is performed based on HBV and intensity information simultaneously in the proposed method. (a) A sketch explains Delaunay triangulation when it is applied based on HBV end points only. (b) When this triangulation is applied based on HBV end points and image intensity simultaneously.

2.C. Automatic segmentation of the liver under HBVs and non-HBVs constraint

Classified HBVs and non-HBVs are used for automatic segmentation of the liver, with the subsequent image resulting from the extraction of bone, accumulated calcium, and kidneys. This process involves fours steps, as described in Fig. 5.

2.C.1. Step 1: Segmenting the core region of the liver

Using the extracted HBVs, a technique based on a two-pass thinning algorithm[49] is applied for extracting center lines of HBVs. End points of HBVs are extracted from this thinning result.[55] Delaunay triangulation[54] is applied to construct a polyhedron structure of the core region of the liver. When this triangulation is constructed based on end points only, end points are connected to each other through lines regardless of positions of these lines in or outside the liver [Fig. 6(a)]. This way of connection may cause segmentation of other organs like the gallbladder. Delaunay triangulation is developed to be applied based on HBV end points and the image (resulting from bone, accumulated calcium, and kidneys removal) intensity on the lines connecting them simultaneously. During this process, the intensity on a line is checked to determine whether it is >20 HU. When this condition is satisfied for all lines of a polygon, this polygon is constructed as a unit of the core region [Fig. 6(b)]. During the construction of ABC in Fig. 6(b), the method checks the intensity of the CT image on the lines connecting the points A, B, and C. Because all of these lines satisfy the condition, ACB will be constructed as a unit of the triangulation. However, the line AE does not satisfy the intensity condition because it passes through a lower intensity region such as the gallbladder or stomach. Therefore, the ACE will not be constructed. All other triangles having the line AE as a side will not be constructed as well. In this way, the proposed method avoids segmentation of regions outside the liver. The value of 20 HU is chosen experimentally based on MICCAI-training data to distinguish between intensities of the gallbladder and LIT. Figure 7 provides an example illustration of such a polyhedron structure of the liver core region.

2.C.2. Step 2: Constructing an initial boundary surface between the liver and other organs

To separate the liver from other organs on CT images, a boundary surface is constructed between the liver and these organs based on the segmented core region and the non-HBV cluster. This surface serves as a boundary between the liver and the neighboring organs at homogenous regions. This boundary surface is perpendicularly and equidistantly constructed in three dimensions between the core region and

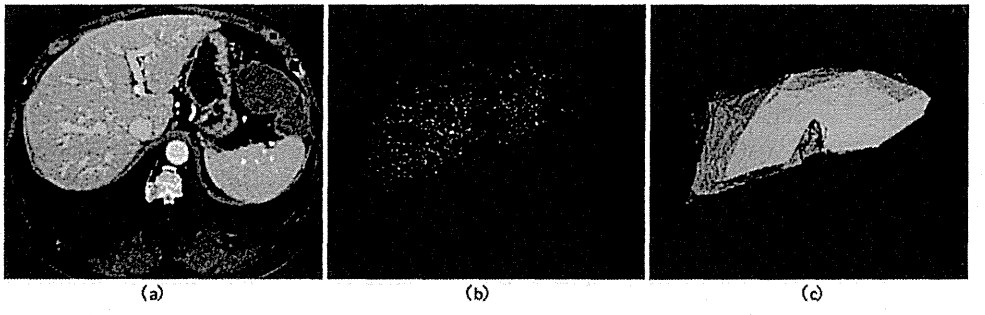

FIG. 7. Example of constructing the polyhedron structure of a liver core region using HBVs and intensity: (a) preprocessed CT dataset (without enhancement) and extracted HBVs, (b) extracted end points of HBVs, and (c) constructed polyhedron structure of the core region.

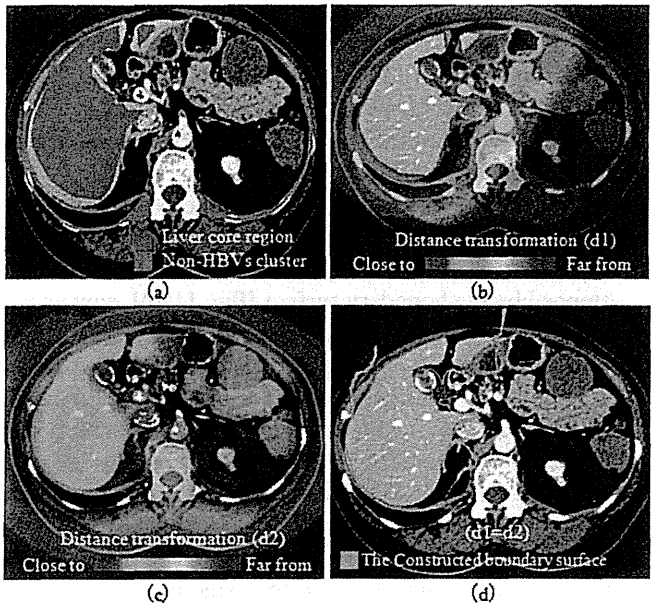

FIG. 8. Boundary surface between the liver and other organs is constructed to separate them when they have similar intensity. (a) Liver core region, non-HBVs cluster are used for constructing this surface (extracted accumulated calcium is marked with arrows). (b) Distance transformation technique is applied starting from the core region to calculate d1. (c) Same technique starting from non-HBVs cluster is applied to calculate d2. (d) The initial boundary surface is constructed at d1 = d2.

the non-HBV cluster. Starting from the core region, a distance transformation technique[52] based on Euclidian distance is used to calculate d1 (p, q), where p and q are two points of three dimensions, p on the surface of the core region and q a point external to the core region. Using the non-HBV cluster only, the same technique is employed to calculate d2 (r, s), where r is a point on the surface of the non-HBVs and s is a point external to the non-HBVs. At places where |d1 − d2| = 0, a perpendicular surface is constructed to separate the two regions. This surface is the initial boundary surface that we construct between the liver and the neighboring organs (Fig. 8).

2.C.3. Step 3: Segmenting LITs

LITs are segmented in two steps: (1) classifying the core region based on its histogram and (2) extending the core region.

2.C.3.a. Step 3.1: Classifying the core region based on its histogram. HBVs and extracted high intensity tumors are removed from the core region. The histogram of the liver core region is calculated. By fitting the histogram using a variational Bayesian Gaussian mixture model.[56] The variational Bayesian inference allows the automatic determination of the number of components in the mixture. The core region is classified based on the number of components of the mixture. When the mixture has one component, a core region is classified as a non-LIT case (NLIT-case). Meanwhile, when the mixture has two components, the core region is classified as a LIT case (LIT-case). LIT-case is classified by dividing the mixture components into two parts: NLIT- and LIT-parts. Figure 9 illustrates the classification of NLIT- and LIT-case core regions.

2.C.3.b. Step 3.2: Extending the core region. To identify the boundary of the liver on CT images, extension is done based on available intensity and the constructed boundary surface. Intensity is employed for extending the core region by

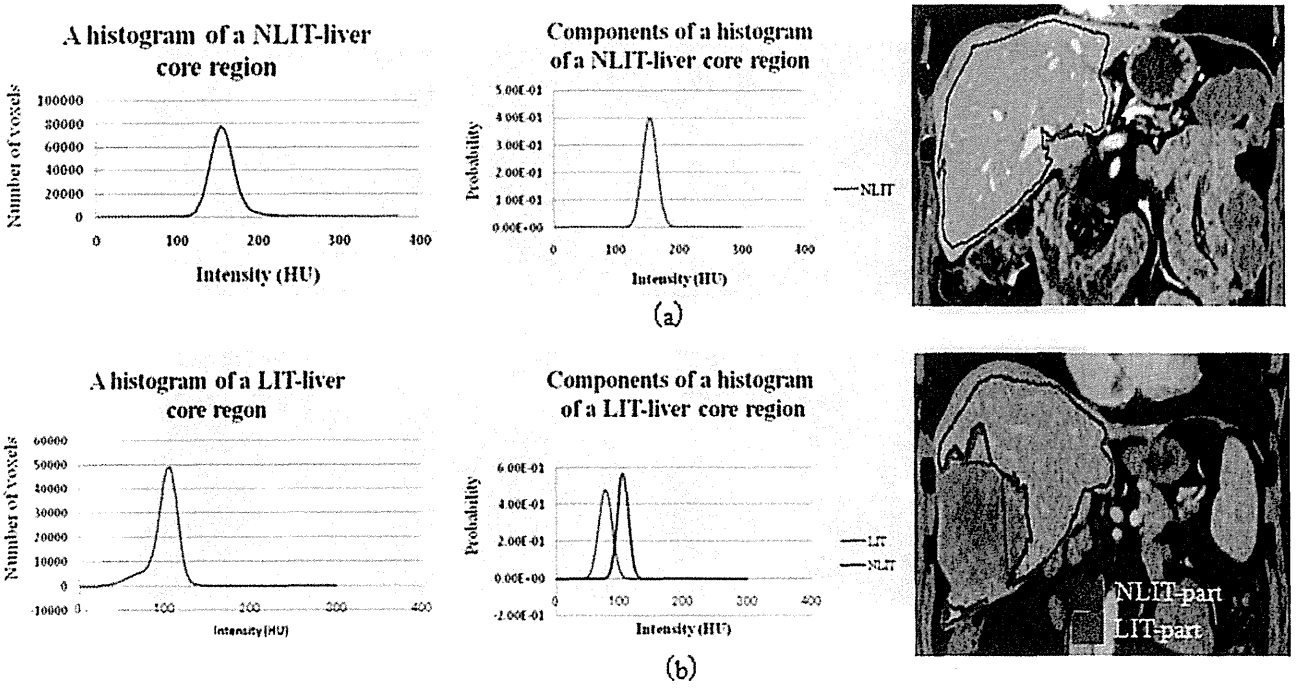

FIG. 9. Two examples of NLIT- and LIT-core regions are classified by fitting their histograms. (Left) Histograms of core regions, (middle) extracted components of each histogram, and (right) core regions are classified into NLIT- and LIT-parts based on their histograms. (a) NLIT-liver (MICCAI-training-15) and (b) LIT-liver (MICCAI-training-16).

FIG. 10. Extension of liver core regions: (a) extension result of a NLIT-case (MICCAI-training-15) and (b) results of a LIT-case, the NLIT- and LIT-parts are segmented separately (MICCAI-training-16).

using the histogram to check the homogeneity of the neighboring regions by checking each voxel. The boundary surface is constructed to separate the liver from neighboring organs when they are similar in intensity.

Extension is achieved via two methods. First, for a core region of a NLIT-case, extension is done based on a single component of the histogram. The component peak is detected. Two thresholds corresponding to 10% of the height of this peak from both sides are selected for this purpose. The core region grows checking neighboring voxels iteratively; when intensities of these neighboring voxels are included in the extension range, these voxels are classified as liver candidates [Fig. 10(a)]. Second, for extending the core region of a LIT-case, the core region is classified into NLIT-and LIT-parts with two corresponding components. Each part of the core region is extended separately using the corresponding component in a similar manner to the extension of the NLIT-case. The NLIT-core region is extended, followed by extension of the LIT [Fig. 10(b)]. NLIT-extension is automatically stopped either when it reaches a variation in intensity between the liver and neighboring regions or when it reaches the boundary surface. Extension of LIT is automatically stopped either when it reaches a variation in intensity or the boundary surface or the extension result of the NLIT-part. HBVs and segmented hepatic tumors are added to the extension result.

In some regions where BVs are not extracted properly, the initial boundary surface intersects the liver causing under-segmentation [Fig. 11(a)]. Therefore when the extension is stopped by the boundary surface [Fig. 11(b)], contact regions between the extension result and this surface are reconfirmed to distinguish between the liver and neighboring organs. A voxel on the initial boundary surface is classified as a voxel of a contact region when one of its 26 neighbors is a voxel of the extension result [Fig. 11(c)]. Contact regions are assigned to different labels. A contact region "a_0" is measured through multiplying number of voxels that is included in this region by the voxel volume. When $a_0 \geq 50$ mm^3, a second boundary surface is constructed in the same manner of the initial boundary surface [Sec. 2.C.2 (Step 2)] using the extension result (instead of the core region) and the non-HBVs cluster [Fig. 11(d)]. The value 50 mm^3 was chosen experimentally to exclude small contact regions from re-extension. The contact region grows checking neighboring voxels iteratively with the second extension range; when intensities of these neighboring voxels are included in the second extension range, these voxels are classified in the extension result [Fig. 11(e)]. This region growing is restricted between the initial and the second boundary surfaces. The second extension range is obtained based on the histogram of the core region and its extension result in the same manner of the first extension range. Contact region [a_1] between first contact region extension and the second boundary surface is obtained. The volume of the first

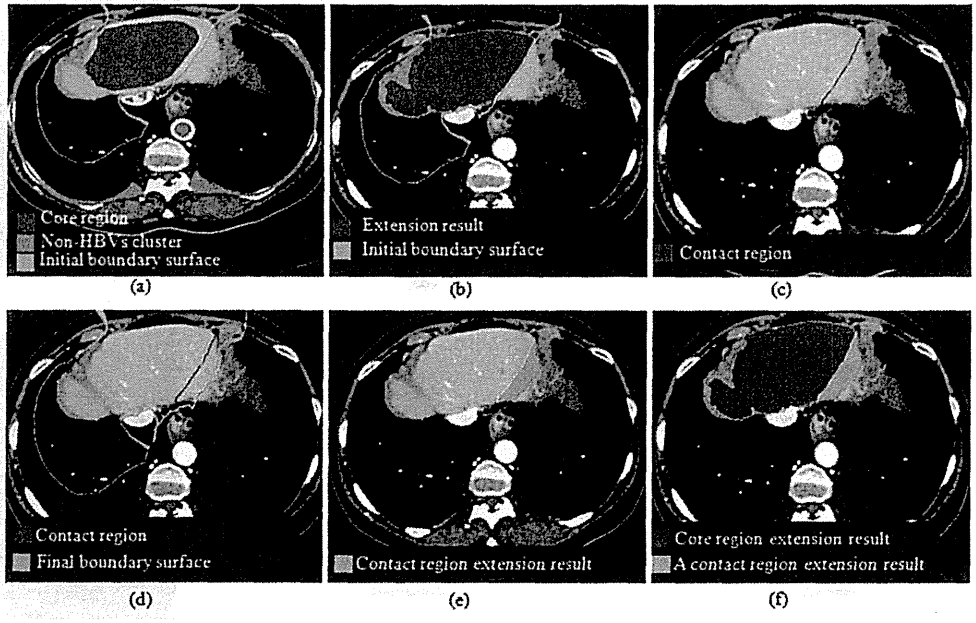

FIG. 11. Reconfirmation of the constructed boundary surface. (a) The initial boundary surface is constructed equidistantly between the core region and non-HBVs cluster. (b) Extension result and the initial boundary surface are used to identify their contact region. (c) Contact region is illustrated. (d) Final boundary surface is constructed between the extension results and non-HBVs cluster. (e) A contact region extension result, and (f) contact region extension result is added to the first extension.